RAMS-forecasts comparison of typical summer atmospheric conditions over the Western Mediterranean coast.

(Atmospheric Research, 2014, 145–146: 130-151.
DOI: 10.1016/j.atmosres.2014.03.018:
http://www.sciencedirect.com/science/article/pii/S0169809514001422)

I. GÓMEZ[a], V. CASELLES[a,b], M. J. ESTRELLA[b,c], R. NICLÒS[a]

[a] *Departament de Física de la Terra i Termodinàmica, Facultat de Física, Universitat de València, Doctor Moliner, 50, 46100 Burjassot, Valencia, Spain.*

[b] *Laboratorio de Meteorología y Climatología, Unidad Mixta CEAM-UVEG, Charles R. Darwin, 14, 46980 Paterna, Valencia, Spain.*

[c] *Departament de Geografia, Facultat de Geografia i Història, Universitat de València, Avda. Blasco Ibáñez, 28, 46010 Valencia, Spain.*

Correspondence to: Igor Gómez Doménech

E-mail: godoi@uv.es

ABSTRACT

The Regional Atmospheric Modeling System (RAMS) has been used in order to perform a high-resolution numerical simulation of two meteorological events related to the most common atmospheric environments during the summer over the Western Mediterranean coast: mesoscale circulations and western synoptic advections. In this regard, we take advantage of the operational RAMS configuration running within the real-time forecasting system environment already implemented over this Mediterranean area, precisely in the Valencia Region and nearby areas. The attention of this paper is especially focused on identifying the main features of both events and the ability of the model in resolving the associated characteristics as well as in performing a comprehensive evaluation of the model by means of diverse meteorological observations available within the selected periods over the area of study. Additionally, as this paper is centred in RAMS-based forecasts, two simulations are operated applying the most two recent versions of the RAMS model implemented in the above mentioned system: RAMS 4.4 and RAMS 6.0. Therefore, a comparison among both versions of the model has been performed as well. Finally, it is our intention to contrast the RAMS forecasts for two completely different atmospheric conditions common with the area of study in the summer. A main difference between the simulation of both meteorological situations has been found in the humidity. In this sense, while the model underestimates this magnitude considering the mesoscale event, especially at night time, the model reproduces the daily humidity properly under the western synoptic advection.

Keywords: RAMS model, operational forecasting, mesoscale modelling, high temperatures, synoptic advection, numerical weather prediction.

1. Introduction

The Regional Atmospheric Modeling System (RAMS) (Cotton et al., 2003; Pielke, 2013) has been running operationally over the Western Mediterranean Basin (Gómez et al., 2010), covering a large extension of eastern Spain, including the whole Valencia Region and surrounding areas, such as the Murcia Region, and its adjacent sea, at a 3 x 3 km grid horizontal resolution (Gómez et al., 2014a; Gómez et al., 2014b).

The most common meteorological framework during the summer months over the Western Mediterranean coast is that corresponding to mesoscale circulations associated with sea-land breezes (Azorin-Molina et al., 2008; Azorin-Molina et al., 2009; Miró et al., 2009; Azorin-Molina et al., 2011), which assumes more than 80% of the situations over eastern Spain (Miró et al., 2009). However, those atmospheric conditions connected to western synoptic advections are also recognized in this region as they are related to high and extreme temperature situations, specially inland but reaching the coast as well (Miró et al., 2006; Estrela et al., 2007; Estrela et al., 2008). Within the summertime, conditions related to western to north-western synoptic advections suppose more than 15% of the total atmospheric situations over eastern Spain (Miró et al., 2009).

Due to the significance of mesoscale circulations over this region in the summer (Miró et al., 2009) and its impact on other environmental issues, such as air pollution, and related human activities (Miao et al., 2003), results stimulating to investigate the forecast of these sort of events using operational configurations of modelling tools. In this regard, mesoscale atmospheric models are remarkably valuable. In addition, the analysis of intense-heat situations, mainly related within the area of study to western synoptic situations (Miró et al., 2006; Estrela et al., 2007; Estrela et al., 2008), is also interesting as they could affect areas as diverse as public health, energy consumption, fauna, flora and natural biodiversity, as well as simple climatic comfort (Estrela et al., 2008).

The main aim of this study is to evaluate and characterize both sort of events and its development over eastern Spain. In this sense, the RAMS configuration used in the real-time operational forecasting system implemented in this area is applied. To deal with this issue, some days were selected during the 2011 summer season operational runs. On one hand, the 25 to 27 June 2011 was chosen as a characteristic sea breeze circulation, which represents a typical summer weather pattern, having weak synoptic forcing and favouring the development of mesoscale processes (Millán et al., 1997; Millán et al., 2000; Palau et al., 2005; Pérez-Landa et al., 2007). On the other hand, the period 25 to 27 August 2011 was selected as a characteristic western synoptic advection (Miró et al., 2006; Estrela et al., 2007; Estrela et. al., 2008). Although the summer 2011 was not specially hot, some periods of high temperatures were recorded. One of them is the one included here, when values of maximum temperatures above 35 ºC were easily reached during the 25 and 26 August throughout the region of study, exceeding 38 ºC in some areas.

In order to study the main features of the sea breeze, such as its intensity, inland penetration and onset, we have taken advantage of both the RAMS 4.4 (RAMS44) and the RAMS 6.0 (RAMS60) configurations running simultaneously within this operational forecasting system. Moreover, a comparison between both RAMS forecasts has been performed as well for the western synoptic advection in order to provide a comprehensive depiction of this episode. This issue will permit to determine and compare the ability of the RAMS model in the prediction of these episodes over the study area. Additionally, the contrast between both RAMS versions will provide an evaluation of the improvements and advantages implemented within the most recent RAMS version when compared to the previous one, originally implemented within this real-time forecasting system.

The paper is structured as follows. Section 2 contains the model configuration and the observational datasets used. In section 3, we introduce the synoptic framework for the selected periods and the model results. Finally, section 4 is devoted to the conclusions of this work.

2. Site description, model set-up and datasets

2.1. Study area

The area of study is bordered by the Mediterranean Sea in its eastern part and surrounded by three main mountain ranges near the coast (Fig. 1). The high terrain in the south and south-west is formed by the Betica Mountains. Their easterly extension, that is, the Pre-Betica range, reaches directly into the sea with cliffs and ridges of more than 700 m. The highest peak inland exceeds 1,500 m. To the north and north-west are the Iberian Mountains with a high ridge and extensive mesas over 2,000 m. Inland of the Valencian Gulf, the mountains are lower, with the highest points reaching 1,100 m, and providing a direct and almost ridgeless rise from the coast to the lower plateau (Millán et al., 2005).

2.2. RAMS model

The atmospheric model used in this study is the RAMS model (Cotton et al., 2003; Pielke, 2013), in its versions 4.4 (RAMS44) and 6.0 (RAMS60). A three modelling domains configuration is adopted following a two-way interactive nesting domain (Fig. 1). The mother domain (D1) covers the southern part of Europe at a 48-km horizontal grid resolution and the Mediterranean. The purpose of the domain is to simulate the synoptic features that influence the region of study. The first nested domain (D2) covers the Iberian Peninsula and the western Mediterranean with a grid resolution of 12 km. Finally, a finer domain (3 km) (D3) includes the Valencia Region at a high horizontal resolution. In the vertical, a 24-level stretched scheme has been selected, with a 50-m spacing near the surface increasing gradually up to 1,000 m near the model top at 11,000 m and with 9 levels in the lower 1,000 m. A summary of the horizontal and vertical grid parameters is provided in Table 1. This configuration for the real-time operational forecasting system was selected as the best compromise for resolving the mesoscale circulations in the Valencia Region within a time frame regarded as useful for the model forecast within the computational resources available.

The configuration employed in the present study incorporates the Mellor and Yamada (1982) level 2.5 turbulence parameterization. Besides, a full-column two-stream single-band radiation scheme that accounts for clouds to calculate short-wave and long-wave radiation (Chen and Cotton, 1983), and the cloud and precipitation microphysics scheme from Walko et al. (1995), apply in all the domains. The Kuo-modified parameterization of sub-grid scale convection processes is used in the coarse domain (Molinari et al., 1985), whereas grids 2 and 3 utilize explicit convection only. Finally, the LEAF-2 soil-vegetation surface scheme (Walko et al., 2000) is used within the RAMS44 environment while LEAF-3 is used for RAMS60. This parameterization permits to calculate sensible and latent heat fluxes exchanged with the atmosphere, using prognostic equations for soil moisture and temperature.

For each of the selected periods, two separate simulations were performed, one accomplished using the RAMS44 configuration and the other one employing the RAMS60 set-up. For the initialization and nudging of the boundaries, the operational global model of the National Centre for Environmental Prediction (NCEP) Global Forecasting System (GFS), at 6 h intervals and 1 x 1 degree resolution globally was used. In addition, a Four-Dimensional Data Assimilation (FDDA) technique was applied to define the forcing at the lateral boundaries of the outermost five grid cells of the largest domain. Each simulation was performed for 84 h, with a temporal resolution of 1 h, starting at 12 UTC 24 June 2011 for the mesoscale framework and at 12 UTC 24 August 2011 for the western synoptic advection. The first 12 h are treated as a spin-up period to avoid possibles problems related to this initialization. Consequently, the analysis will be performed using the remaining 72-h.

2.3. Observational datasets

The results obtained from the different RAMS simulations are compared to the observations considering the finer domain (D3). On the one hand, 4 automatic surface weather stations from the CEAM (Mediterranean Center for Environmental Studies) Foundation network (Corell-Custardoy et al., 2010) and representative of the model results in the area of study are considered in the analysis. This 4 meteorological stations are divided in 3 corresponding to inland locations and the other 1 related to a coastal site (Fig. 1). On the other hand, the Murcia synoptic METAR station data (MUR; Fig. 1) is included for verification of the model output as well. In addition, as MUR is also a regular radiosonde station, the corresponding sounding at this site is also ready for use.

Hourly measures of near-surface temperature, relative humidity, wind speed and direction from the CEAM and METAR stations are used in the validation process. Additionally, the surface incident shortwave radiation flux from the CEAM network is used as well. Likewise, vertical profiles for temperature and relative humidity corresponding to the 00Z and 12Z MUR soundings are included in the evaluation procedure.

3. Results and discussion

3.1. Synoptic analysis

To describe the synoptic configuration under the two atmospheric frameworks, the NCEP FNL (Final) Operational Global Analysis at 12Z have been used (Fig. 2). The FNLs are made with the same model which NCEP uses in the Global Forecast System (GFS), but the FNLs are prepared about an hour or so after the GFS is initialized. The FNLs are delayed so that more observational data can be used (NCEP, 2013). On the one hand, the Iberian Thermal Low (ITL; Millán et al., 1997; Millán et al., 2000; Palau et al., 2005) is developed on the 25 June 2011 (Fig. 2a). The next day (Fig. 2b), this low pressure influences the west part of the Iberian Peninsula and remains moving to the east the 27 June. On the other hand, a high pressure centre affects the north of Spain the 25 June, that is displaced to the centre of Europe for the following days. The 26 and the 27 June, this high pressure affects mainly the centre and east part of Spain extending to the Mediterranean and Europe. In contrast, the west of the Iberian Peninsula is under the influence of relative low pressures associated with the low pressure over the British Islands. At 500 hPa, it is shown that fair weather conditions are established over the Iberian Peninsula, influenced by high pressures and the -10ºC isotherm positioned over this area. Under this atmospheric framework, mesoscale circulations are expected over eastern Spain.

Fig. 3 contains the sea level pressure and the surface wind field simulated by RAMS44 and RAMS60 for the 26 June 2011 in the domain D2. Before down, at 06 UTC, a relative high pressure dominates over the Iberian Peninsula (Fig. 3a,b), with slight lower values simulated by RAMS44. In terms of the simulated wind flow, a rather similar pattern is found when comparing both versions of RAMS. In addition, over the east coast of Spain, variable weak winds are well-established. At noon (Fig. 3c,d), the ITL is settled over the centre of the Iberian Peninsula, coinciding to the warm conditions at that time. Under these conditions, a sea breeze circulation develops covering the whole east coast of Spain. This surface pattern is recognized by both versions of the model. However, it seems that a rather slight higher pressure is once again simulated by RAMS60. This result could be related to the differences in intensity found in some areas, where RAMS44 is more windy than RAMS60 (see also section 3.3).

According to this results, it is clear that at 12 km resolution (D2), we are able to see the differences in the wind field pattern between day and night time. In addition, Fig. 3 permits identify to what extent the local pressure organization produces mesoscale circulations along the east coast of Spain. In this regard, it is seen that surface drainage winds are oriented from land to sea at night time. In contrast, thermal circulations develop during the day, and a distinct flow pattern regime is stabilized, advecting air from sea to land.

Regarding the western synoptic advection, on the 25 August, there is an upper level low pressure located west of Ireland, while a low pressure dominates in the surface over the Iberian Peninsula (Fig. 2c). This atmospheric framework favours the development of a western wind flow over the east coast of the Iberian Peninsula. On the 26 August, the upper level low pressure is slightly displaced to the east, passing across the British Islands and affecting the north-west of the Iberian Peninsula (Fig. 2d). In addition, a secondary relative low pressure centre is located over the Balearic Islands, affecting the east coast of Spain. Simultaneously, the pressure organization at low levels favours the development of strong winds from the west to north-west crossing the Iberian Peninsula and reaching the Mediterranean (not shown). Besides, a warm air ridge from the Sahara extends over the Mediterranean, affecting the western basin sideways. Under such synoptic conditions, a well-developed western advection is formed over the Iberian Peninsula.

For the 26 August 2011 at 06 UTC, a slight pressure gradient over the Iberian Peninsula is simulated by RAMS in the domain D2, with lower values over the Mediterranean, favouring a western wind flow over the east coast of Spain (Fig. 3e,f). Although some differences are reproduced when comparing RAMS44 with RAMS60, the same basic structure is simulated by both versions of the model (Fig. 3e,f). However, more differences are produced at day time. In this regard, at 12 UTC (Fig. 3g,h), a lower pressure is simulated by RAMS44. Nevertheless, the atmospheric framework is similar using RAMS44 and RAMS60, characterized by a descending surface pressure gradient from the west of the Iberian Peninsula to the east, which boosts a visible synoptic western advection over this area.

3.2. Comparison between model and measurements

To evaluate the model skill, several statistical indexes has been computed (Tables 2 and 3). The statistical calculations carried out in both cases include the mean bias, root mean square error (RMSE) and index of agreement (IoA) for temperature, relative humidity and wind speed. Besides, the observed averaged value and modelled averaged value are computed, for these variables, the wind direction and the incident surface flux of shortwave radiation, for graphical depiction purposes. In addition, for the wind direction variable, we have computed the root mean square error for the vector wind direction (RMSE-VWD).

As we are evaluating RAMS forecasts, we include additional variables at this point in order to investigate whether other RAMS-computed variables improve the model skill in terms of surface variables, such as the 2-m temperature and the 10-m wind speed. In this regard, both variables calculated by the model are directly compared to the observations as well. Considering the model's ability to reproduce the western synoptic advection, although the whole simulation is presented, the main discussion is focused on the western advection recorded the 26 August. Consequently, while computing the different statistical scores, only the available data within the 24-h on 26 August are considered (Table 3).

Fig. 4 includes the near-surface wind speed and direction, and the 10-m wind speed during the mesoscale circulation period and the western synoptic conditions. The diurnal evolution of the simulated wind direction clearly demonstrates that not only is RAMS properly capturing the onset and the closure of the sea breeze but also the development of the corresponding mechanism. This result is reproduced in all weather stations. Additionally, although at night time the observed wind speed values are very low, we must highlight that the model is still able to simulate the observed wind direction suitably, with north-west to north directions. The western synoptic advection basically dominates the 26 August in the whole region (Fig. 4b,d,f), with the exception of the northern coastal area of the Valencia Region, where the sea breeze is still able to develop (Fig. 4h). At BEN station, we can see a difference between the 25 and 26 August. In the first case, a mesoscale sea-land breeze is well-established. In the second case, the onset of the wind sea breeze is delayed in comparison to the 25 August due to the intensity of the western flow over the region. However, the sea breeze breaks this flow in the end, and dominates the atmospheric situation during the day. In both cases, RAMS is able to reproduce the mentioned wind flow changes accurately. Likewise, in those stations where the dominant wind field is the corresponding western advection, RAMS properly captures the wind pattern observed using the two versions of the model. Under both atmospheric conditions, the model shows more differences in a more complex terrain (Fig. 4a,b). These divergences may be related to the model not being able to reproduce suitably the physical characteristics of the area where the station is located. As a result, the differences in orography between the model and the real location can influence the channelling of the wind field in the area. Nevertheless, the RMSE-VWD presents values between 2-3 m/s under the mesoscale circulation period, lower for the RAMS60 simulation when compared to the RAMS44 results.

Regarding the near-surface wind speed, the model displays a trend to overestimate the observations during the day time and using both versions of RAMS during the mesoscale period (Fig. 4). In general, RAMS60 produces lower values than RAMS44, remaining closer to the observations. During the night, the model reproduced better the recorded wind speed compared to the results found for the day time (Fig. 4). However, RAMS reproduces really well the observations during the day during the western synoptic advection (Fig. 4). In both cases, the different statistics computed show that the accuracy of the model rises when using the 10-m wind speed compared to the near-surface wind speed computed at 10 m (Tables 2 and 3). In general, the RMSE for the near-surface wind direction is in between 1 and 2 m/s and the IoA reflects that RAMS captures the day-to-day evolution of this magnitude properly.

The daily evolution of near-surface wind speed and direction and the 10-m wind speed at MUR METAR station is included in Fig. 6a for the mesoscale circulation period and in Fig. 6e for the western synoptic advection. In both case, we observe similar results to those found for the CEAM surface stations (Fig. 4). However, although the observations show a western flow on 26 August, the model reproduces a southern flow for some hours, coinciding with an overestimation of the simulated wind speed.

The observed and simulated daily evolution for the near-surface temperature, 2-m temperature and near-surface relative humidity is introduced in Fig. 5 for the mesoscale circulation period and the western synoptic advection. Regarding temperature, RAMS is able to capture the diurnal variation amplitude, as indicated by the high values of the IoA, above 0.8 in general (Tables 2 and 3), and using both RAMS44 and RAMS60. Comparing the different versions of the model as well as the near-surface temperature and the 2-m temperature, it seems that the last one shows a general trend towards overestimating the observed maximum temperatures while the near-surface temperature reproduces this magnitude properly during the western synoptic advection. Additionally, in terms of minimum temperatures, and as a difference with the simulation of mesoscale circulations, under the western synoptic forcing, RAMS is able to capture the daily minimum with a greater degree of accuracy.

The diurnal variation of the relative humidity clearly shows the development of the sea breeze (Fig. 5). In all stations, this parameter computed at daytime is well captured by the model, specially taking into account the RAMS60 simulation. However, at night, there is a deficit of the modelled relative humidity compared to the one measured. This point seems to be a pattern reproduced for the whole region, specially over inland areas, as may be seen in Fig. 5a. In contrast, considering pure coastal stations (Fig. 5g), this issue is not so clear, and the difference is not that high. In addition, in pre-coastal stations, the model's ability to predict the relative humidity field is in between that found for the coast and inland (not shown). Regarding the whole simulation, a clear negative bias is found for all stations using both versions of the model (Table 2). However, RAMS60 produces lower values of this statistic when compared to the RAMS44 version. In this sense, the model presents some difficulties in forecasting this field, as a systematic error is found, with a clear tendency to underestimate the observations. In addition, the IoA shows these difficulties as well, as values between 0.5 and 0.7 are reproduces by the model using both versions. If we compare the relative humidity observed on the 25 August and that observed on the 26 August, we may see significant differences, specially at night time. Although under mesoscale conditions an elevated humidity is observed within this period of the day, the relative humidity observed under a western synoptic advection is significantly low. In terms of relative humidity (Table 3), even though the Bias still shows negative values as in it is observed under sea breeze conditions, lower values are found for this statistical score. In addition, Fig. 5 shows that the model is closer to the observations the 26 August. Furthermore, an overestimation of the RAMS-simulated relative humidity is observed in some locations, as indicated by positive values in the Bias score. We must remark at this point that RAMS is able to capture rather well the diurnal evolution of this magnitude, as shown in values for the IoA higher than 0.8. Consequently, under this western advection, the model in general follows the observed daily evolution properly. During this period and regarding VIS station, it was mentioned before that RAMS does not capture the wind direction observed properly. However, both the temperature and the relative humidity tend to follow the results found for the other weather stations (Fig. 5a). This finding seems to indicate that the model is strongly influenced by the western synoptic advection. The simulated interface produced by the meeting of the two mentioned regimes could be the responsible for the accuracy found in terms of temperature and the relative humidity, even though the wind pattern is displaced to the east. Besides, the complex orography of the VIS site in addition to the heterogeneity of the wind field over this area could also be related to the divergences between the model and the measurements for this magnitude. Finally, Fig. 6b,f shows the correspondence with the CEAM data (Fig. 5).

Considering the surface incident shortwave radiation flux (Fig. 7), it is notably well reproduced by the model in all weather stations, as indicated by the values of IoA, equal to 1 using both versions of the model (Tables 2 and 3). However, during the western synoptic advection, more differences appear between the observations and the

RAMS results in some stations. In this case, the observations seem to indicate the presence of cloudiness that is not reproduced by the model (Fig. 7f,h). Under the mesoscale circulation, the bias presents positive values in general below 30 W/m^2, while RMSE presents values between 60-70 W/m^2 (Table 2). In this case, RAMS reproduces really well the daily heating (Fig. 7). In contrast, the simulated values for the daily cooling show an overestimation in relation to the observations. In this sense, it seems that the modelled cooling rate is lower that the one recorded, which could have its implication in the temperature and relative humidity differences described above.

Considering Fig. 6, we evaluate the vertical profiles at MUR site as illustrative of the vertical structure of the sea breeze period and the western synoptic advection. In the first case, both at 00 and 12 UTC, a stratification is observed for temperature (Fig. 6c) and relative humidity (Fig. 6d). The Atmospheric Boundary Layer (ABL) height distribution shows a boundary layer structure well defined with a mixing height of approximately 1,000 m. At 00 UTC, the vertical profile displays an inversion layer at this point and an abrupt change in the relative humidity. This inversion is also observed at 12 UTC, when the sea breeze circulation is establish, but it is weaker than the one reproduced at 00 UTC. Fig. 6d shows that beneath the mixing height, both RAMS44 and RAMS60 underestimate the observations at 00 and 12 UTC. However, higher differences are observed at night time. In both cases, RAMS60 is higher than RAMS44, being closer to the observations at 12Z, while still substantially apart from them at 00Z. Besides, although RAMS is not able to capture this inversion layer properly, it still shows a change in the vertical profiles at the height of about 1,000 m, where the inversion layer is observed. In addition, RAMS60 properly simulates the vertical structure below the 1,000 m, with the corresponding boundaries slightly below the observations. Furthermore, the model still captures the change in the temperature trend observed at higher levels. Finally, the temperature vertical profile at MUR under the influence of the western synoptic advection is included in Fig. 6g. Both the model and the observations shows a clear stratification under 2,000 m. In addition, it is shown that the model reproduces remarkably well the observations on 27 August at 00 UTC. Besides, on 26 August at 12 UTC, RAMS44 follows perfectly the observed vertical temperature, while RAMS60 slightly underestimates this magnitude. The vertical profile for the relative humidity represented under this atmospheric condition (Fig. 6h), indicates an opposite trend as the one observed under mesoscale circulations (Fig. 6d). Although in the last case, RAMS produces a significant underestimation of the observed relative humidity at night time, under a western advection, the model slightly overestimates this magnitude in the lowest levels within this period of the day. When modelling this atmospheric framework using RAMS, the RAMS60 simulation perfectly matches the observations in the lowest vertical levels during the day, while RAMS44 slightly underestimates this magnitude.

3.3. Horizontal structure

In this section, not only the simulated wind field is included, but also we are interested in the evolution of the simulated near-surface relative humidity and temperature evolution. In this regard, the 26 June 2011 have been selected as representative day for the study of the mesoscale circulations during the sea breeze event. Nevertheless, similar results are found considering both the 25 and the 27 June 2011.

Fig. 8 displays the relative humidity and the wind field at 06 and 18 UTC for the 26 June and the 26 August. This figure presents some temporal and spatial variabilities reflecting several significant features of the sea breeze system. The nocturnal wind pattern is dominated by a weak flow mainly blowing from the west to north-west (Fig.

8a,b). This flow is identified as a land breeze circulation. In the afternoon (Fig. 8c,d), the sea breeze is completely developed, reaching areas located at inland distances larger that 70-80 km beyond the coast. A difference is found in the sea breeze flow between the north, the south and the centre of the Valencia Region. It is observed that in the centre of this area, an eastern flow is established. In contrast, north of the Valencia Region, a more southern flow is maintained reaching nearby inland areas. Finally, south of the Valencia Region and the neighbour Murcia Region, a south-east flow is settled. This flow joint together with the eastern flow developed in the centre of the area of study produces a convergence line moving from the coast to inland areas due to the orographic configuration (Fig. 1).

The observational hourly evolution of the sea breeze (Fig. 4) indicates that the 08 UTC is fixed as the onset of the sea breeze. In general, the model captures this time as the beginning of this circulation precisely, as described in the previous section. However, in some stations, there seems to be a delay of about 1 hour. An inspection of the simulated wind direction (not shown) makes evident that the wind begins to blow onshore at about 07 UTC in the north of the Valencia Region, while the sea breeze develops over the whole coastline of the area of study at 08 UTC. One hour later, the sea breeze is reaching pre-coastal areas near the coast. As the simulation progresses, as shown in Fig. 8, there is an onshore wind advection that moves towards inland locations. In this sense, at 18 UTC (Fig. 8c,d), there is a clear sea breeze system spreading to the interior. It seems that this time distinguish the hour when this mesoscale circulation reaches its maximum spatial development. Finally, at about 19-20 UTC, the sea breeze system starts weakening while the mountain circulations become the dominant flow over this area in the nocturnal hours (Fig. 4).

In terms of the near-surface relative humidity, higher values are observed at night when contrasting with the values recorded during the day. However, as it was shows in the previous section, the tendency of the model is to underestimate the records of this magnitude. Comparing RAMS44 with RAMS60, once again, the first one simulates lower values than the last one for the whole simulation (Fig. 8). Some divergences are found among both version regarding the wind field, specially during the day time. In this sense, it seems that RAMS44 moves the convergence line formed in the centre-south of the Valencia Region to the north.

Considering the near-surface temperature (Fig. 9), although, as it was seen in Section 3.2, minimum temperatures are overestimated by the model, the maximum temperatures are well reproduced by RAMS60, while RAMS44 tends to over-predict the observed values. It appears that under mesoscale circulations related to sea breeze development, temperatures with values higher than 30 ºC are observed in the Valencia Region (Gómez et al., 2014a; Gómez et al., 2014b), specially in the central pre-coastal area and the south of the region. Even though the temperature distribution during the day time is similar for both versions of the model, once again, RAMS44 produces higher values than RAMS60 for the whole simulation.

In Fig. 8, the near-surface wind field and relative humidity is also represented for the western synoptic event. On 26 August, where the western advection dominates, some divergences are found at 06 UTC (Fig. 8e,f). Comparing RAMS44 and RAMS60, the first one is able to reach coastal areas at this time, as it is also represented in the relative humidity structure. On the contrary, both this magnitude and the wind field reflect unsteady calm winds over the coast while the western advection remains inland. The relative humidity separates these atmospheric flows, with lower humidity in those areas where the western advection dominates and higher values near the coast. At 18

UTC (Fig. 8g,h)., RAMS44 as well as RAMS60 reproduces a western advection that reaches the coast in the centre of the Valencia Region. In the north, the sea breeze is still able to develop, as it was indicated in the previous section in Fig. 4. In this case, mesoscale circulations are limited to areas close to the coast, while inland the western flow governs the atmospheric situation. However, according to observations (Fig. 4b), it appears that the western to north-western synoptic advection was able to drive into coastal areas, further than reflected by the model. As a difference with other areas, a south advection is well-established in southern areas. Consequently, a convergence line is formed due to the connection between this southern flow and the western to north-western advection at about 38.5º N. In terms of temperature, two areas of really high temperatures are detected in Fig. 9g,h, where its distribution spreads affecting coastal areas within the Valencia Region.

Finally, Fig. 10a,b shows the surface sensible heat flux distribution at 15 UTC, when the sea breeze circulation is well established. The sensible heat flux pattern is related to the wind field evolution (not shown). It is well known that the difference in the first one is a critical factor in producing and modifying mesoscale circulations (Miao et al., 2003). In this sense, areas with high values for the sensible heat flux match up with areas where the sea breeze is well established. Consequently, the sea breeze, mainly driven by sensible heat flux differences, seems to enhance the sensible heat flux over land by advecting air masses from the adjacent sea, as onshore winds advect cool and moist air near the surface (Miao et al., 2003). Comparing both versions of RAMS, RAMS44 produces higher values of the sensible heat flux than those observed for RAMS60. In addition, it is observed that using RAMS44, high values for the sensible heat flux, above 500 W/m^2, are simulated at 15 UTC, while significant lower values are reproduced by RAMS60. These results could be the responsible for the differences observed in the simulated wind field and near-surface temperature.

The above mentioned differences between RAMS44 and RAMS60 for the 26 August are also well reflected in terms of the surface sensible heat flux. This magnitude is displayed in Fig. 10c,d at 15 UTC. The change in the surface sensible heat flux distinguishes the contrasting weather regimes present over the Western Mediterranean coast. On the one hand, those areas where the breeze is well-established shows values above 400 W/m^2 (Fig. 10a,b). On the other hand, those areas where the western advection governs the atmospheric framework show values around 300 W/m^2 and lower (Fig. 10c,d). In this regard, an obvious distinction is found between both weather regimes adopting the surface sensible heat flux. Furthermore, looking at the southern area represented in Fig. 10c,d, we are able to recognize an area of high sensible heat flux, above 400 W/m^2. As it was indicated previously, a southern wind flow is organized over this area, advecting warm air through the sea towards the coast. This issue represents a major divergence between the corresponding circulation in this area and that observed in the centre and north of the Valencia Region. In this last case, continental warm air is advected across the Iberian Peninsula to the eastern areas of Spain. In contrast, south-eastern Spain seems to be dominated by an advection of warm air through the Mediterranean Sea, as it is also observed in the differences in relative humidity among both concrete areas (Fig. 8). Finally, comparing the surface sensible heat flux simulated by RAMS44 and RAMS60, the results are rather alike. However, more variability is produced adopting the RAMS44 version of the model. In addition, RAMS44 shows higher values for this magnitude as well.

3.4. Vertical structure

In order to reflect the evolution of the vertical circulation, we have selected a latitude cross section to represent the relative humidity and the horizontal winds at a latitude of 39.45º (Fig. 11), corresponding to the Valencia Bay, during both the mesoscale circulation period and the western synoptic advection. At 06 UTC (Fig. 11a,b), there is a weak flow from the north-west flow moving offshore. In this period, the land breeze is still activated for both RAMS44 and RAMS60. However, some divergences arise. For instance, at longitude -0.9º, weaker winds are simulated by RAMS44 in addition to a different development in the wind direction when compared to RAMS60. At 18 UTC (Fig. 11c,d), the sea breeze continues and a divergence between RAMS44 and RAMS60 in the magnitude of the simulated flow is settled onshore. In this sense, RAMS44 appears to move inland and with an increased intensity. In the afternoon, it is clear the difference that evolves for the relative humidity field, specially near the coast, as it was already indicated in Fig. 5.

Fig. 11 also displays the relative humidity and horizontal wind vectors in a vertical cross section at 39.45ºN considering RAMS model D3 on 26 August at 06 and 18 UTC. At 06 UTC (Fig. 11e,f) the western wind flow strengthens at upper levels. Below 900 m, the wind regime is characterized by a marked north-western component reaching the coast. In addition, when comparing RAMS44 with RAMS60, it is exposed to view the differences in relative humidity near the coast, specifically in the lowest 300 m. This issue turns into a notorious contrast in the wind speed within this layer affected by high relative humidity and a weak circulation. At 18 UTC (Fig. 11g,h), the current flow is disposed as a western synoptic advection reaching the coast. In this case, the sea breeze is limited to the coastal barrier, where mesoscale circulations are confined to the lowest 300 m. Onshore, the wind regime is characterized by an explicit western advection covering all vertical levels, starting from the ground-based level. In this regard, alike conclusions are obtained contrasting RAMS44 and RAMS60.

4. Conclusions

The main aim of this paper has been to investigate the main features of a typical mesoscale circulation system, as well as a typical western synoptic advection over eastern Spain during the summer. Both sort of meteorological conditions have been analysed using an operational configuration of the RAMS model.

Combining measurements and model forecasts, we have been able to recognize that the main processes and the spatial flow patterns observed under the mesoscale circulation regimes are captured with high accuracy both by RAMS44 as well as RAMS60. Accordingly, RAMS simulates the wind field suitably, especially using the RAMS60 version. Likewise, RAMS60 predicts better the near-surface minimum temperature as well as the near-surface relative humidity observed at night time. Besides, it has been observed that RAMS60 tends to simulate higher values of near-surface relative humidity and lower values of near-surface temperature than those produced by RAMS44. In addition, RAMS is able to capture quite well the maximum temperatures under sea breeze conditions. However, in some areas, there is a trend to overestimate this magnitude using RAMS44.

Some discrepancies are found in terms of the night-time near-surface relative humidity, which is translated into an overestimation in the minimum temperature. Under sea breeze circulations, the model underestimates the relative humidity at night. The differences found between the model and the observations are larger for RAMS44. A possible reason for this deviation may be related to the data used to initialize the RAMS model. Additionally, this constraint may also be probably related to the nocturnal cooling of the ground which could not be satisfactorily simulated by the model. In this regard, it is well known that landscape and terrain heterogeneities induce spatially varying surface turbulent fluxes, resulting in heterogeneous boundary layers (Pielke, 2013). Therefore, further tests and analysis should be performed so as to isolate this issue.

The observed relative humidity vertical profile shows a mixing height at about 1,000 m during the mesoscale circulation. Under this level, there is a clear underestimation of the relative humidity simulated by the model, which seems to be correlative with the results found near the ground. Additionally, although the observed vertical profile for the temperature shows a stratified layer up to around 1,000 m, the profile solved by the model shows stability, specially using RAMS44. However, RAMS60 remains closer to the observations, producing stratification for those vertical levels near the surface. In general, RAMS60 improves the results obtained with RAMS44 below the ABL.

Regarding the western synoptic advection, although the model is able to capture adequately the diurnal variation of those stations near the northern coast, it has more difficulties in forecasting the inland wind pattern observed. Nevertheless, even in this area, the model is still able to reproduce the recorded relative humidity and temperature accurately. Concerning the first magnitude, RAMS captures its daily evolution. In addition, a slight overestimation is simulated by the model at night time. This is an evident difference when compared to the results obtained under mesoscale circulations. As a consequence, the minimum temperature is also better forecast by the model. Additionally, RAMS captures truly well the inland maximum temperatures. Comparing this magnitude simulated by RAMS44 and RAMS60, the last one show lower values than RAMS44, in general closer to the observations, but slightly underestimating the observations on occasion. The opposite trend is observed for the relative humidity.

The temperature vertical profiles under the western synoptic advection shows a high agreement between the model and the measurements both at night and day time, using both versions of the model. Furthermore, the vertical relative humidity is truly well simulated by RAMS60, specially at day time, although RAMS44 shows a slight divergence from the observations. Additionally, at night time, RAMS shows a weak overestimation of the relative humidity in the lowest levels. Once again, we can see here a main difference in the RAMS-based forecasts between western advections and mesoscale circulations related to the relative humidity. Considering that issue, it seems to be a direct connection between the RAMS model output and the separate simulation of both episodes.

The conclusions identified in the present study for the mesoscale circulation event, in terms of the wind speed and direction, are comparable to those found in related diagnostic studies performed over reduced areas in eastern Spain and using older versions of the RAMS model (see e.g., Millán et al., 2000; Miao et al., 2003; Pérez-Landa et al., 2007).

Although some disagreement has been found using the RAMS configuration presented in this paper when predicting humidity due to the complexity of the modelled system as well as the constraints expected in an operational forecasting environment, it is very encouraging to notice as well that RAMS is able to reproduce reliably the main mesoscale flows observed. However, in light of the results found in the relative humidity, it seems that further investigation should be performed in the future with the aim of improving the RAMS forecasts under mesoscale conditions. On the other hand, it has been shown that the current implementation of the RAMS model over eastern Spain has been truly useful in the forecast of the western synoptic advection event.

Acknowledgement

This work has been funded by the Regional Government of Valencia through the contract “Simulación de las olas de calor e invasiones de frío y su regionalización en la Comunitat Valenciana” (“Heat wave and cold invasion simulation and their regionalization at the Valencia Region”) and the project PROMETEO/2009/086, and by the Spanish Ministerio de Economía y Competitividad through the project CGL2011-30433. The authors wish to thank D. Corell for providing the CEAM weather station data. NCEP is acknowledged for providing the GFS meteorological forecasts for RAMS initialization as well as the FNL analysis data. National Centers for Environmental Prediction/National Weather Service/NOAA/U.S. Department of Commerce (2000): NCEP FNL Operational Model Global Tropospheric Analyses, continuing from July 1999. Research Data Archive at the National Center for Atmospheric Research, Computational and Information Systems Laboratory. Dataset. http://rda.ucar.edu/datasets/ds083.2. Accessed 25 Nov 2013. National Climatic Data Center (NCDC) is acknowledged as well for providing the METAR data. Finally, the authors acknowledge the Atmospheric Soundings portal of the University of Wyoming (http://weather.uwyo.edu/upperair/sounding.html) for providing the radiosonde data.

References

Azorin-Molina C, Lopez-Bustins JA (2008). An automated sea breeze selection technique based on regional sea-level pressure difference: WeMOi. International Journal of Climatology 28: 1681–1692. doi: 10.1002/joc.1663.

Azorin-Molina C, Chen D (2009). A climatological study of the influence of synoptic-scale flows on sea breeze evolution in the Bay of Alicante (Spain). Theoretical and Applied Climatology 96: 249–260. doi: 10.1007/s00704-008-0028-2.

Azorin-Molina C, Chen D, Tijm S, Baldi M (2011). A multi-year study of sea breezes in a Mediterranean coastal site: Alicante (Spain). International Journal of Climatology 31: 468–486. doi:10.1002/joc.2064.

Chen, C, Cotton, WR (1983). A one-dimensional simulation of the stratocumulus-capped mixed layer. Boundary-Layer Meteorology 25: 289–321.

Corell-Custardoy D, Valiente-Pardo JA, Estrela-Navarro MJ, García-Sánchez F, Azorín-Molina C (2010). Red de torres meteorológicas de la Fundación CEAM (CEAM meteorological station network). 2nd Meeting on Meteorology and Climatology of the Western Mediterranean, Valencia, Spain.

Cotton WR, Pielke RAS, Walko RL, Liston GE, Tremback CJ, Jiang H, McAnelly RL, Harrington JY, Nicholls ME, Carrio GG, McFadden JP (2003). RAMS 2001: Current status and future directions. Meteorology and Atmospheric Physics 82 (1-4): 5-29.

Estrela M, Pastor F, Miró J, Gómez I, Barberà M (2007). Heat waves prediction system in a mediterranean area (valencia region). 7th EMS Annual Meeting / 8th European Conference on Applications of Meteorology.

Estrela M, Pastor F, Miró J, Gómez I, Barberà M (2008). Diseño de un sistema de predicción operativa de niveles de riesgo por temperaturas extremas para la Comunidad Valenciana. Olas de calor. In: Estrela, MJ (Ed.). Riesgos climáticos y cambio global en el Mediterráneo español. ¿Hacia un clima de extremos?. Colección Interciencias, UNED, pp. 235-252.

Gómez I, Estrela MJ (2010). Design and development of a java-based graphical user interface to monitor/control a meteorological real-time forecasting system. Computers & Geosciences 36: 1345-1354. doi:10.1016/j.cageo.2010.05.005.

Gómez I, Estrela, MJ, Caselles, V (2014a). Operational forecasting of daily summer maximum and minimum temperatures in the Valencia Region. Natural Hazards 70(2): 1055-1076, doi: 10.1007/s11069-013-0861-1.

Gómez I, Caselles, V, Estrela, MJ (2014b). Real-time weather forecasting in the Western Mediterranean Basin: An application of the RAMS model. Atmospheric Research 139: 71-89, doi: 10.1016/j.atmosres.2014.01.011.

Mellor G, Yamada T (1982). Development of a turbulence closure model for geophysical fluid problems. Reviews of Geophysics and Space Physics 20: 851-875.

Miao J-F, Kroon LJM, Vilà-Guerau de Arellano J, Holtslag AAM (2003) . Impacts of topography and land degradation on the sea breeze over eastern Spain. Meteorolology and Atmospheric Physics 84: 157–170.

Millán, MM, Salvador, R, Mantilla, E, Kallos G (1997). Photooxidants dynamics in the Mediterranean basin in summer: Results from European research projects. Journal of Geophysical Research 102(D7): 8811–8823.

Millán MM, Mantilla E, Salvador R, Carratalá A, Sanz MJ, Alonso L, Gangoiti G, Navazo M (2000). Ozone cycles in the Western Mediterranean basin: Interpretation of monitoring data in complex coastal terrain, Journal of Applied Meteorology 39 (4): 487–508.

Millán, MM, Estrela, MJ, Miró, J (2005). Rainfall components: variability and spatial distribution in a Mediterranean area. Journal of Climate. 18: 2682–2705.

Miró JJ, Estrela MJ, Millán MM (2006). Summer temperature trends in a mediterranean area (valencia region). International Journal of Climatology 26: 1051-1073.

Miró J, Estrela MJ, Pastor F, Millán M (2009). Análisis comparativo de tendencias en la precipitación, por distintos inputs, entre los dominios hidrológicos del Segura y del Júcar (1958-2008), in Spanish. Investigaciones Geográficas 49: 129-157.

Molinari J. 1985. A general form of kuo's cumulus parameterization. Monthly Weather Review 113: 1411-1416.

NCEP (2013). National Centers for Environmental Prediction/National Weather Service/NOAA/U.S. Department of Commerce (2000): NCEP FNL Operational Model Global Tropospheric Analyses, continuing from July 1999. Research Data Archive at the National Center for Atmospheric Research, Computational and Information Systems Laboratory. Dataset. http://rda.ucar.edu/datasets/ds083.2. Accessed 25 Nov 2013.

Palau JL, Pérez-Landa G, Diéguez JJ, Monter C, Millán MM (2005). The importance of meteorological scales to forecast air pollution scenarios on coastal complex terrain. Atmospheric Chemistry and Physics 5: 2771-2785.

Pérez-Landa G, Ciais P, Sanz MJ, Gioli B, Miglietta F, Palau JL, Gangoiti G, Millán M (2007). Mesoscale circulations over complex terrain in the Valencia coastal region, Spain. Part 1: Simulation of diurnal circulation regimes. Atmospheric Chemistry and Physics 7: 1835-1849.

Pielke Sr. RA (2013). Mesoscale meteorological modeling. 3rd Edition. Academic Press, San Diego, CA, 760 pp.

Walko RL, Cotton WR, Meyers MP, Harrington JY (1995). New RAMS cloud microphysics parameterization. Part I: The single-moment scheme. Atmospheric Research 38: 29-62.

Walko RL, Band LE, Baron J, Kittel TGF, Lammers R, Lee TJ, Ojima D, Pielke RA, Taylor C, Tague C, Tremback CJ, Vidale PL (2000). Coupled atmospheric-biophysics-hydrology models for environmental modeling. Journal of Applied Meteorology 39: 931-944.

Figure captions

Fig. 1. Configuration of the three nested domains and orography (m) of the RAMS model on domain D1 in addition to the weather station sites and orography for the finer domain (D3).

Fig. 2. Sea level pressure (hPa, solid line), geopotential height (gpm, shaded color) and temperature in ºC (dashed line) at 500 hPa from FNL global model at 12 UTC on 25 June (a), 26 June (b), 25 August (c) and 26 August (d) 2011.

Fig. 3. Sea level pressure (hPa, solid line), wind (arrows; scale: 10 m/s) an orography on domain D2 at 06 UTC: RAMS44 (a), RAMS60 (b), and at 12 UTC: RAMS44 (c), RAMS60 (d) the 26 June 2011 and at 06 UTC: RAMS44 (e), RAMS60 (f), and at 12 UTC: RAMS44 (g), RAMS60 (h) the 26 August 2011.

Fig. 4. Measured (continuous line) and simulated (discontinuous line) near-surface wind speed (m/s) and direction (deg), and 10-m wind speed (m/s) time series, for different surface weather stations during the mesoscale circulation period: VIS (a), VIL (c), UTI (e), and BEN (g), and under the synoptic western advection: VIS (b), VIL (d), UTI (f), and BEN (h)

Fig. 5. Same as Fig. 4, but for the near-surface temperature (ºC) and relative humidity (%), and 2-m temperature (ºC).

Fig. 6. Same as Fig. 4 (a) and same as Fig. 5 (b), but for the MUR METAR station over the mesoscale circulation period, as well as over the western synoptic advection (e) and (f). Measured (continuous line) and simulated (discontinuous line) vertical profiles on 26 June at at 00 UTC and 12 UTC: temperature (ºC; c), relative humidity (%; d), and on 26 August at 12 UTC and on 27 August at 00 UTC: temperature (ºC; g), relative humidity (%; h).

Fig. 7. Same as Fig. 4, but for the surface incident shortwave radiation flux (W/m^2).

Fig. 8. Simulated near-surface wind field (scale: 10 m/s) and relative humidity (%) on domain D3 on 26 June 2011 at 06 UTC: RAMS44 (a), RAMS60 (b), on 26 June 2011 at 18 UTC: RAMS44 (c), RAMS60 (d), on 26 August 2011 at 06 UTC: RAMS44 (e), RAMS60 (f), and on 26 August 2011 at 18 UTC: RAMS44 (g), RAMS60 (h).

Fig. 9. Same as Fig. 8, but for the near-surface temperature (ºC).

Fig. 10. Simulated surface sensible heat flux (W/m^2) over domain D3 on 26 June 2011 at 15 UTC: RAMS44 (a), RAMS60 (b), and on 26 August 2011 at 15 UTC: RAMS44 (c), RAMS60 (d).

Fig. 11. Vertical variation of simulated horizontal wind field (m/s) and relative humidity (%) for a cross-section at latitude 39.45º N on 26 June 2011 at 06 UTC: RAMS44 (a), RAMS60 (b), on 26 June 2011 at 18 UTC: RAMS44 (c), RAMS60 (d), on 26 August 2011 at 06 UTC: RAMS44 (e), RAMS60 (f), and on 26 August 2011 at 18 UTC: RAMS44 (g), RAMS60 (h).

Tables

Table 1. Rams model settings for the three simulation grids: number of grid points in the x, y and z directions (nx, ny and nz), horizontal grid spacing (dx) and timestep (t).

Grid	nx	ny	nz	dx (m)	t (s)
1	83	58	24	48,000	60
2	146	94	24	12,000	30
3	78	126	24	3,000	10

Table 2. Model skill against surface observations under the mesoscale event for the whole simulation and the representative stations. Index of agreement, Bias and RMSE are included for the near-surface temperature (T; ºC), 2-m temperature (T2m; ºC), relative humidity (RH; %), wind speed (WS; m/s), 10-m wind speed (WS10m; m/s) and surface incident shortwave radiation flux (RAD; W/m^2), in addition to the RMSE-VWD (VWD; m/s).

Site	Statistic variable	RAMS44			RAMS60		
		IoA	Bias	RMSE	IoA	Bias	RMSE
VIS	T	0.8	5	5	0.8	3	5
	T2m	0.9	-4	5	0.9	4	4
	RH	0.5	-30	40	0.5	-30	30
	WS	0.8	1.4	1.7	0.8	1.5	1.7
	WS10m	0.9	0.4	0.8	0.9	0.8	1.0
	VWD	-	-	2	-	-	2
	RAD	1.0	21	60	1.0	30	70
VIL	T	0.9	3	4	0.9	0.07	3
	T2m	1.0	-0.19	3	0.9	1.8	3
	RH	0.6	-30	40	0.7	-19	30
	WS	0.8	1.1	2	0.9	0.5	1.5
	WS10m	0.9	0.6	1.3	0.9	0.09	1.1
	VWD	-	-	3	-	-	2
	RAD	1.0	11	70	1.0	16	70
UTI	T	0.9	5	5	0.9	1.0	3
	T2m	1.0	-0.2	3	0.9	2	3
	RH	0.7	-20	24	0.8	-13	18
	WS	0.8	1.6	2	0.8	0.9	1.4
	WS10m	0.9	0.9	1.4	0.9	0.3	0.9
	VWD	-	-	3	-	-	2
	RAD	1.0	17	70	1.0	30	80
BEN	T	0.9	0.9	2	0.8	-1.8	3
	T2m	0.8	4	5	0.9	-0.8	1.9
	RH	0.6	-18	23	0.6	-9	18
	WS	0.8	1.6	2	0.9	0.6	1.1
	WS10m	0.8	1.0	1.5	1.0	0.02	0.6
	VWD	-	-	3	-	-	1.8
	RAD	1.0	22	70	1.0	30	70
MUR	T	0.6	3	4	0.8	0.4	3
	T2m	0.5	7	8	0.6	3	5
	RH	0.3	-40	40	0.3	-30	30
	WS	0.6	0.9	3	0.7	0.08	2
	WS10m	0.6	0.9	2	0.7	-0.16	1.9

Table 3. Model skill against surface observations for the 26 August 2011 and the representative stations. Index of agreement, Bias and RMSE are included for the near-surface temperature (T; ºC), 2-m temperature (T2m; ºC), relative humidity (RH; %), wind speed (WS; m/s), 10-m wind speed (WS10m; m/s) and surface incident shortwave radiation flux (RAD; W/m^2), in addition to the RMSE-VWD (VWD; m/s).

831

Site	Statistic variable	RAMS44			RAMS60		
		IoA	Bias	RMSE	IoA	Bias	RMSE
VIS	T	0.9	2	4	0.9	1.8	4
	T2m	0.7	-7	8	0.9	3	3
	RH	0.7	-12	20	0.7	-8	18
	WS	0.5	0.07	2	0.5	0.7	3
	WS10m	0.5	-0.9	2	0.5	-0.3	2
	VWD	-	-	7	-	-	7
	RAD	1.0	50	100	1.0	50	100
VIL	T	0.8	1.9	4	0.8	0.4	4
	T2m	0.9	-2	4	0.9	1.6	4
	RH	0.6	-12	19	0.9	-5	10
	WS	0.9	-0.5	1.1	0.9	-0.5	1.2
	WS10m	0.9	-0.9	1.2	0.9	-0.8	1.3
	VWD	-	-	1.9	-	-	1.5
	RAD	1.0	14	80	1.0	17	80
UTI	T	0.8	3	5	0.8	2	4
	T2m	0.9	-2	5	0.9	3	4
	RH	0.6	-10	19	0.7	-7	15
	WS	1.0	0.6	1.0	0.9	0.05	1.1
	WS10m	0.9	-0.2	0.9	0.9	-0.6	1.4
	VWD	-	-	1.7	-	-	2
	RAD	1.0	40	100	1.0	40	100
BEN	T	0.8	-2	3	0.6	-3	4
	T2m	0.9	0.7	3	0.8	-1.9	3
	RH	0.9	4	16	0.8	18	22
	WS	0.7	0.7	1.8	0.8	0.05	1.2
	WS10m	0.7	0.15	1.6	0.8	-0.6	1.4
	VWD	-	-	5	-	-	5
	RAD	1.0	50	100	1.0	50	100
MUR	T	1.0	-0.2	2	0.9	-1.4	3
	T2m	1.0	0.9	1.7	1.0	-0.15	1.0
	RH	0.7	-14	24	0.9	-5	16
	WS	0.5	1.9	3	0.5	1.2	3
	WS10m	0.6	1.0	2	0.5	0.6	2

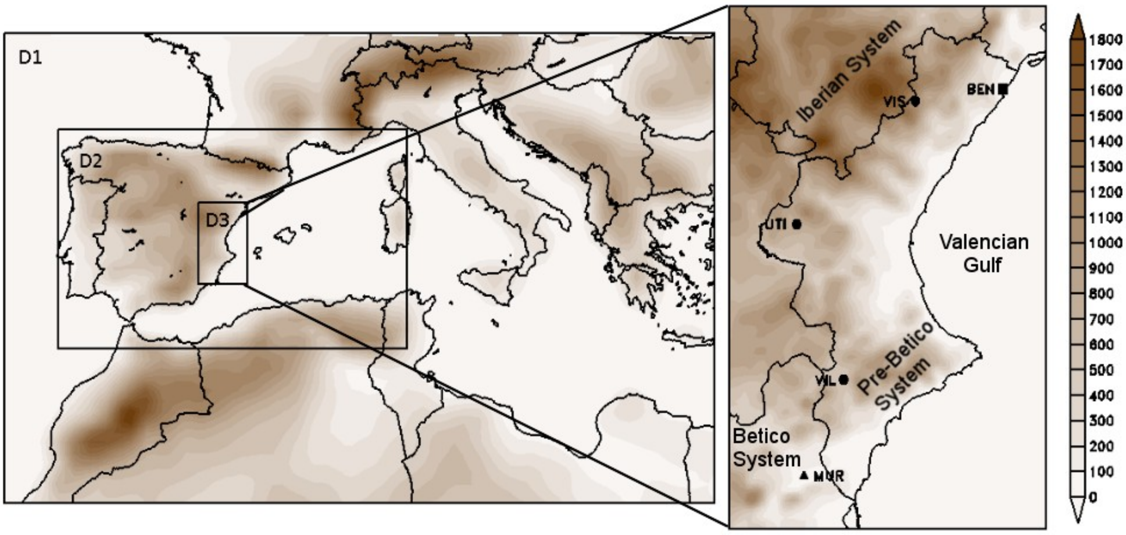

Figure 1

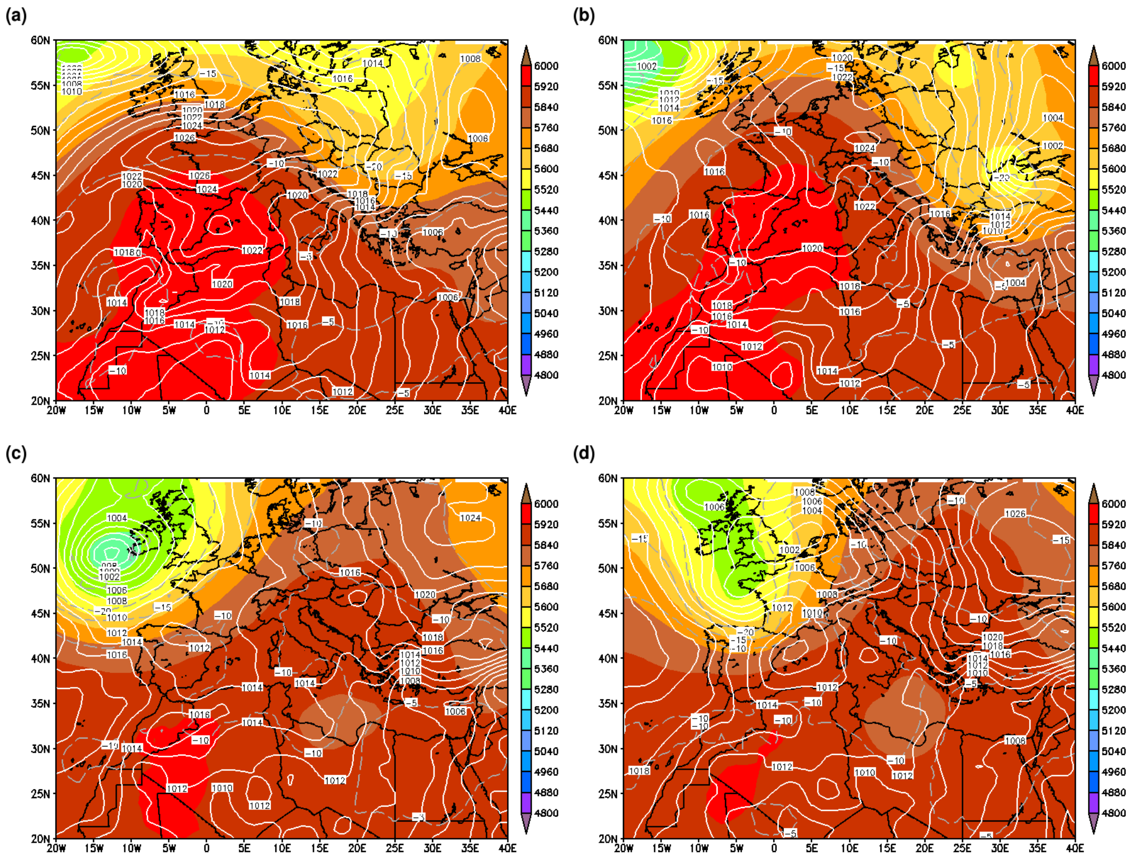

Figure 2

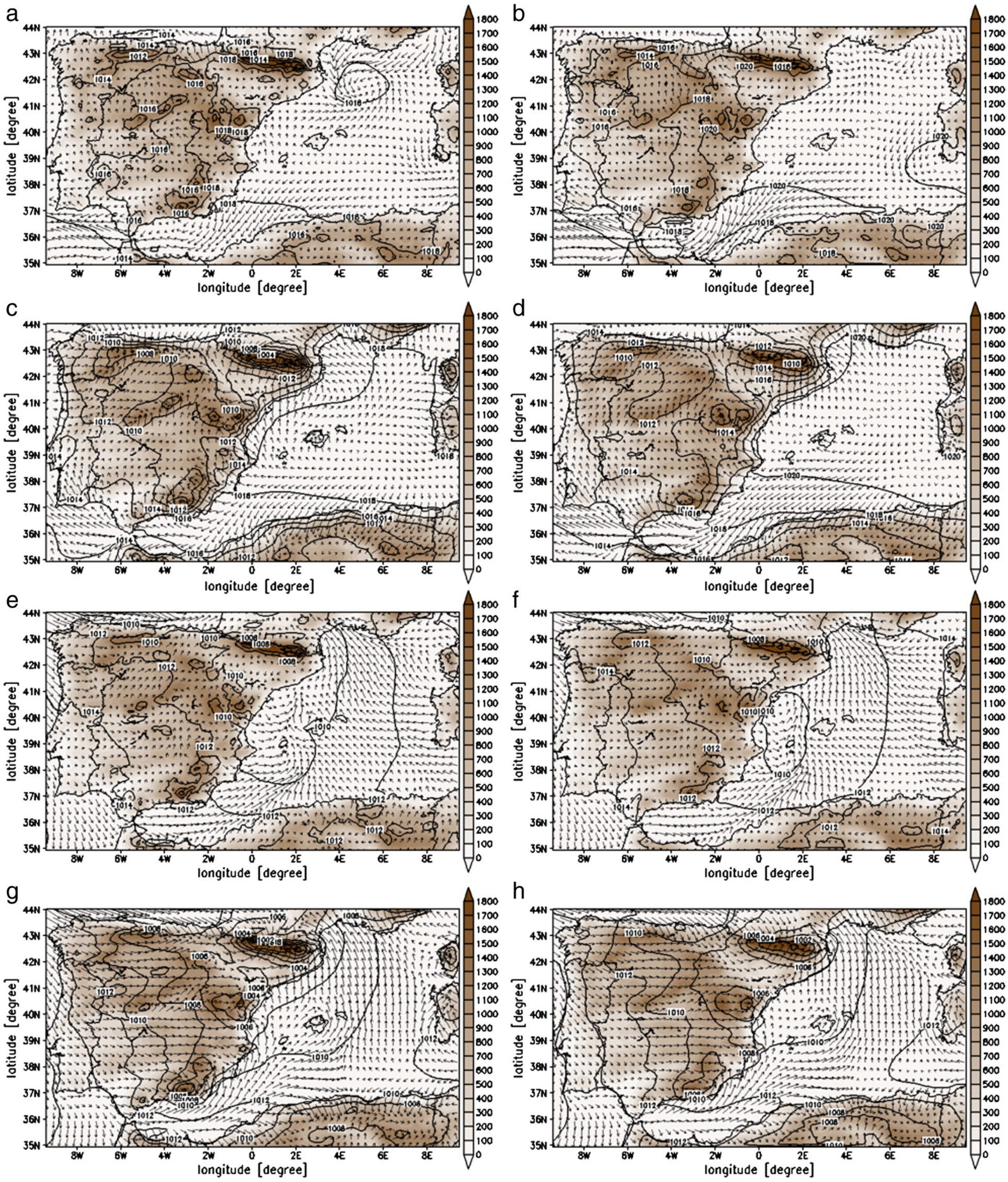
a
b
c
d
e
f
g
h
latitude [degree]
longitude [degree]
44N
43N
42N
41N
40N
39N
38N
37N
36N
35N
8W
6W
4W
2W
0
2E
4E
6E
8E
1800
1700
1600
1500
1400
1300
1200
1100
1000
900
800
700
600
500
400
300
200
100
0

Figure 3

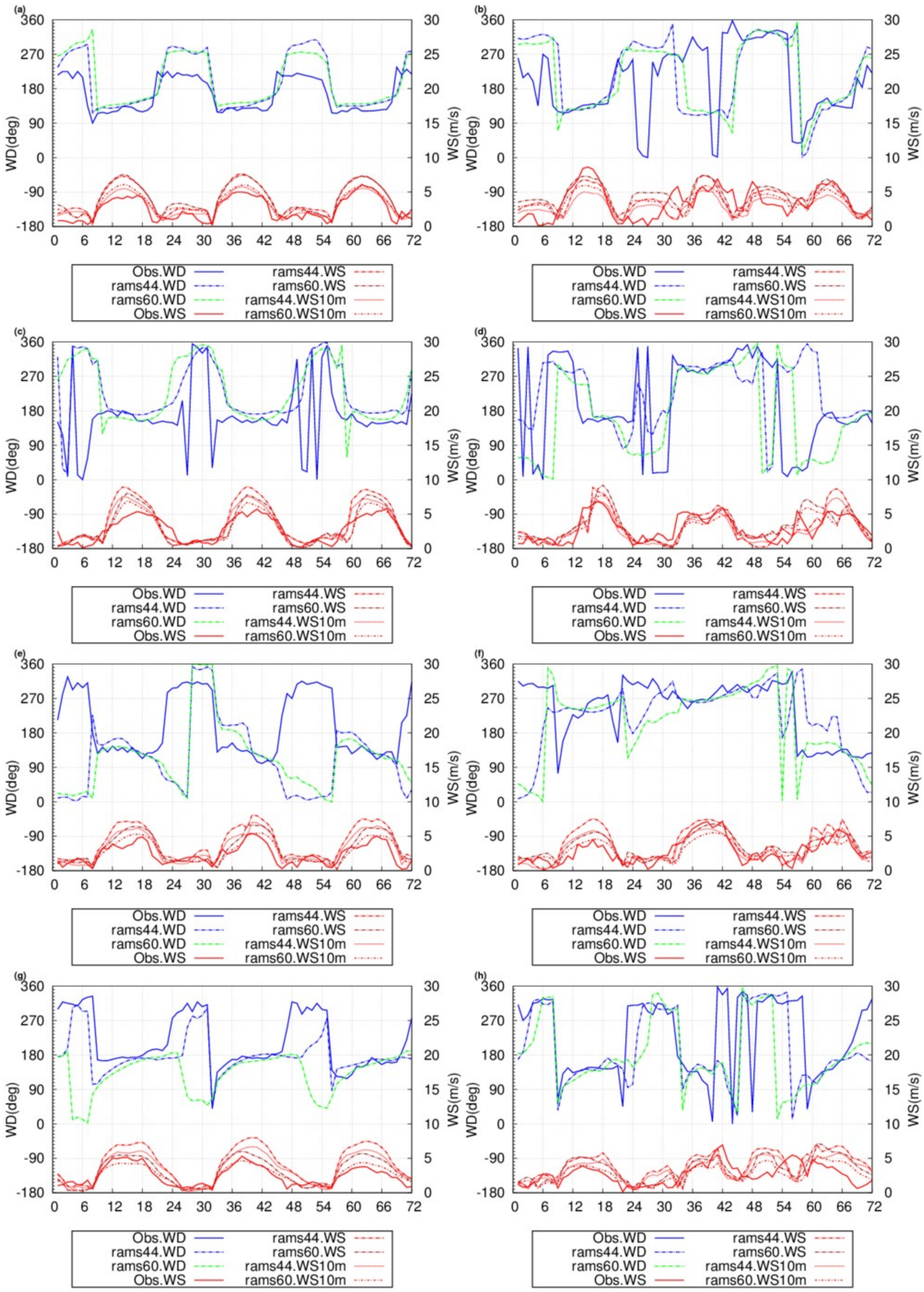
(a)
(b)
(c)
(d)
(e)
(f)
(g)
(h)
WD(deg)
WS(m/s)
360
270
180
90
0
-90
-180
30
25
20
15
10
5
0
0 6 12 18 24 30 36 42 48 54 60 66 72
Obs.WD
rams44.WD
rams60.WD
Obs.WS
rams44.WS
rams60.WS
rams44.WS10m
rams60.WS10m

Figure 4

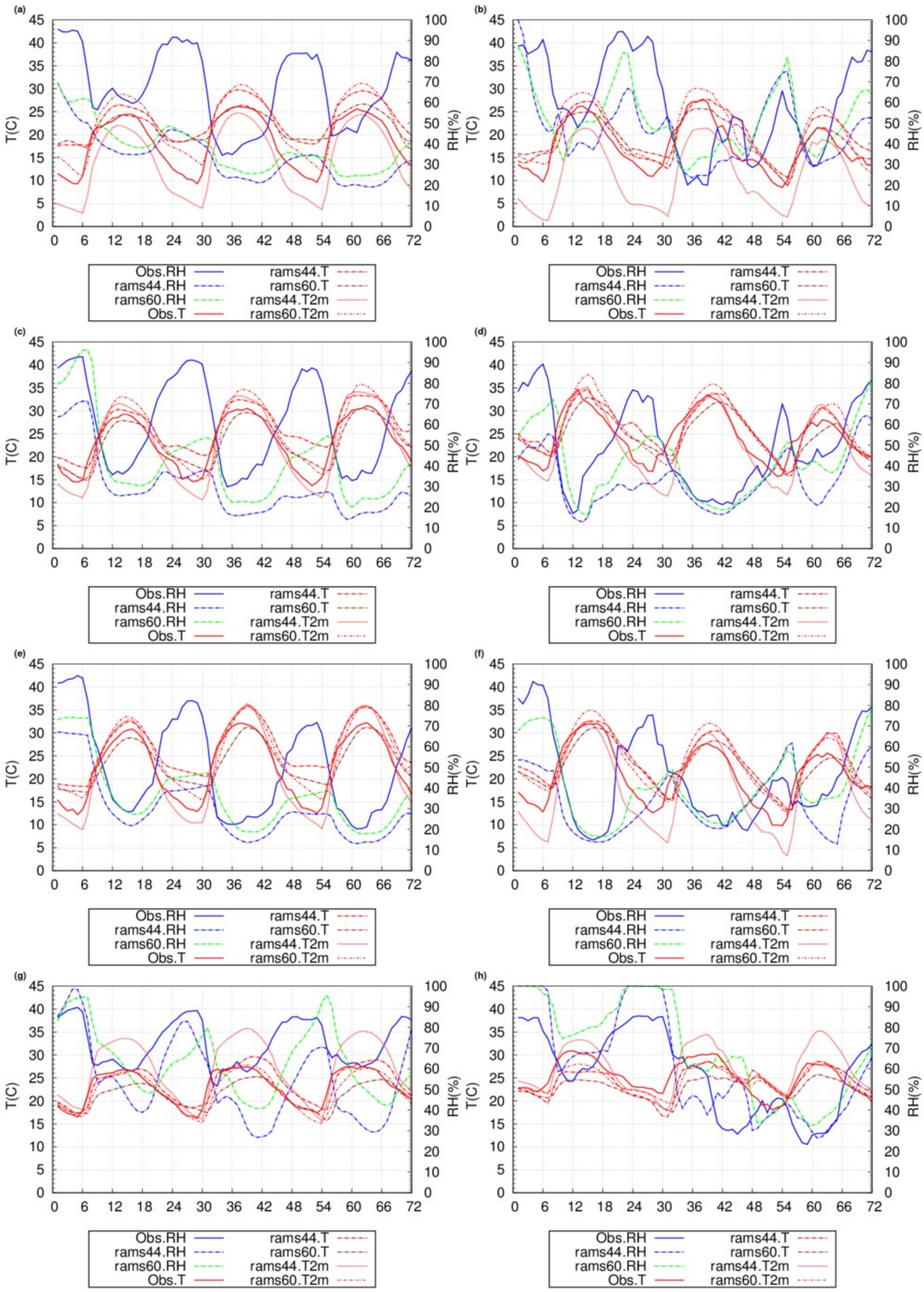
(a)
(b)
(c)
(d)
(e)
(f)
(g)
(h)
T(C)
RH(%)
Obs.RH
rams44.RH
rams60.RH
Obs.T
rams44.T
rams60.T
rams44.T2m
rams60.T2m

Figure 5

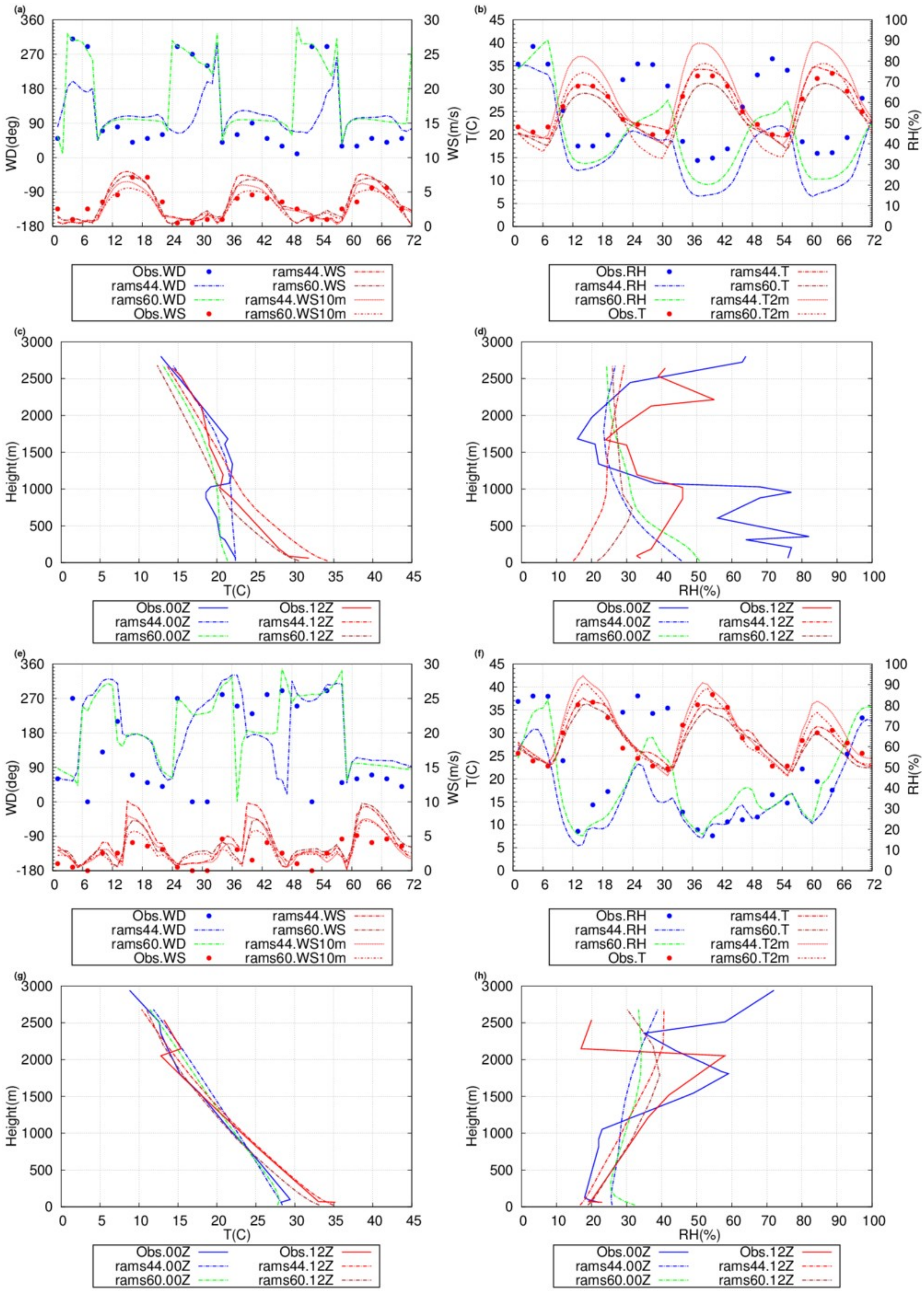
(a)
WD(deg)
WS(m/s)
Obs.WD
rams44.WD
rams60.WD
Obs.WS
rams44.WS
rams60.WS
rams44.WS10m
rams60.WS10m
(b)
T(C)
RH(%)
Obs.RH
rams44.RH
rams60.RH
Obs.T
rams44.T
rams60.T
rams44.T2m
rams60.T2m
(c)
Height(m)
T(C)
Obs.00Z
rams44.00Z
rams60.00Z
Obs.12Z
rams44.12Z
rams60.12Z
(d)
Height(m)
RH(%)
Obs.00Z
rams44.00Z
rams60.00Z
Obs.12Z
rams44.12Z
rams60.12Z
(e)
WD(deg)
WS(m/s)
Obs.WD
rams44.WD
rams60.WD
Obs.WS
rams44.WS
rams60.WS
rams44.WS10m
rams60.WS10m
(f)
T(C)
RH(%)
Obs.RH
rams44.RH
rams60.RH
Obs.T
rams44.T
rams60.T
rams44.T2m
rams60.T2m
(g)
Height(m)
T(C)
Obs.00Z
rams44.00Z
rams60.00Z
Obs.12Z
rams44.12Z
rams60.12Z
(h)
Height(m)
RH(%)
Obs.00Z
rams44.00Z
rams60.00Z
Obs.12Z
rams44.12Z
rams60.12Z

Figure 6

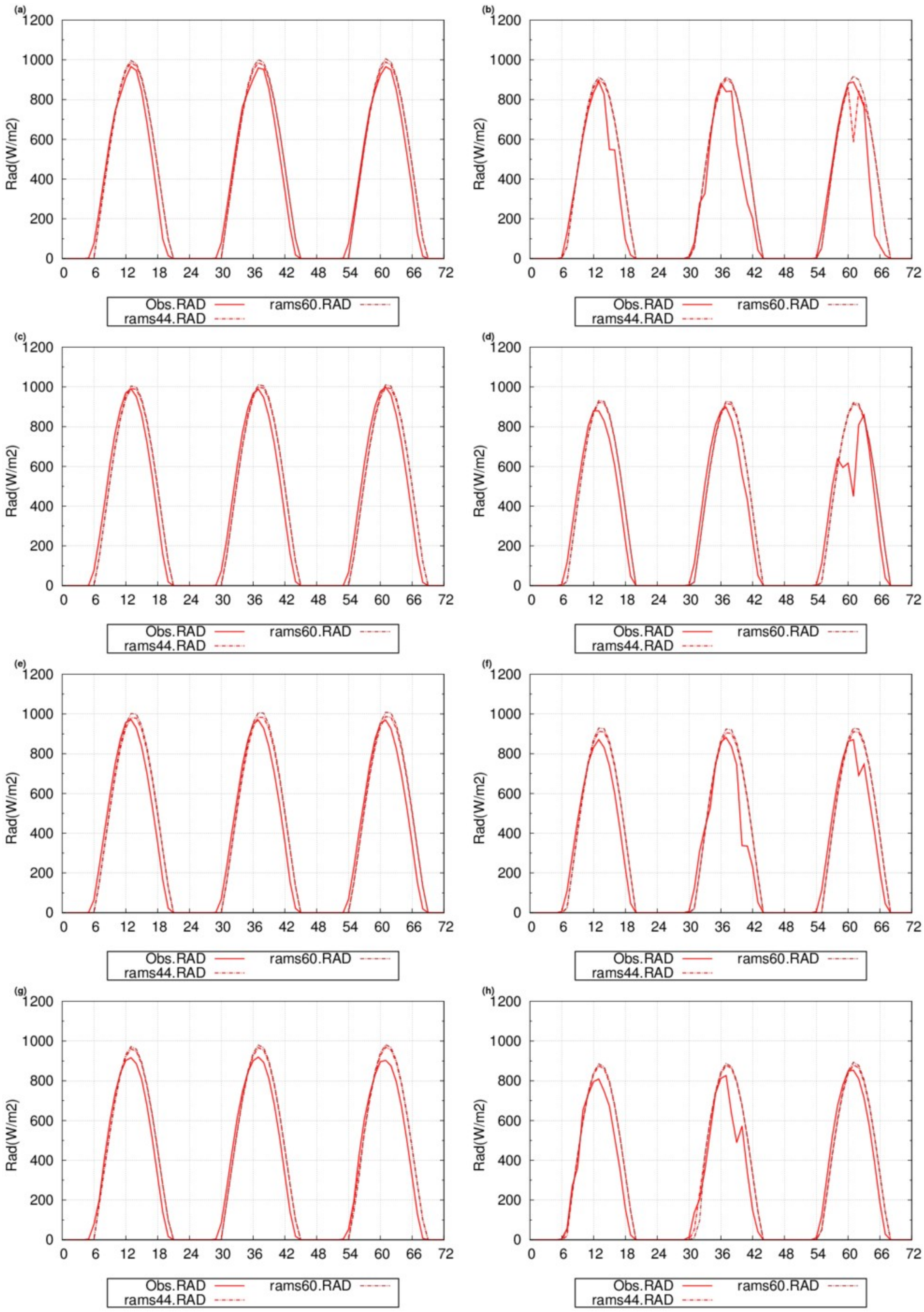
(a)
(b)
(c)
(d)
(e)
(f)
(g)
(h)
Rad(W/m2)
0 200 400 600 800 1000 1200
0 6 12 18 24 30 36 42 48 54 60 66 72
Obs.RAD
rams60.RAD
rams44.RAD

Figure 7

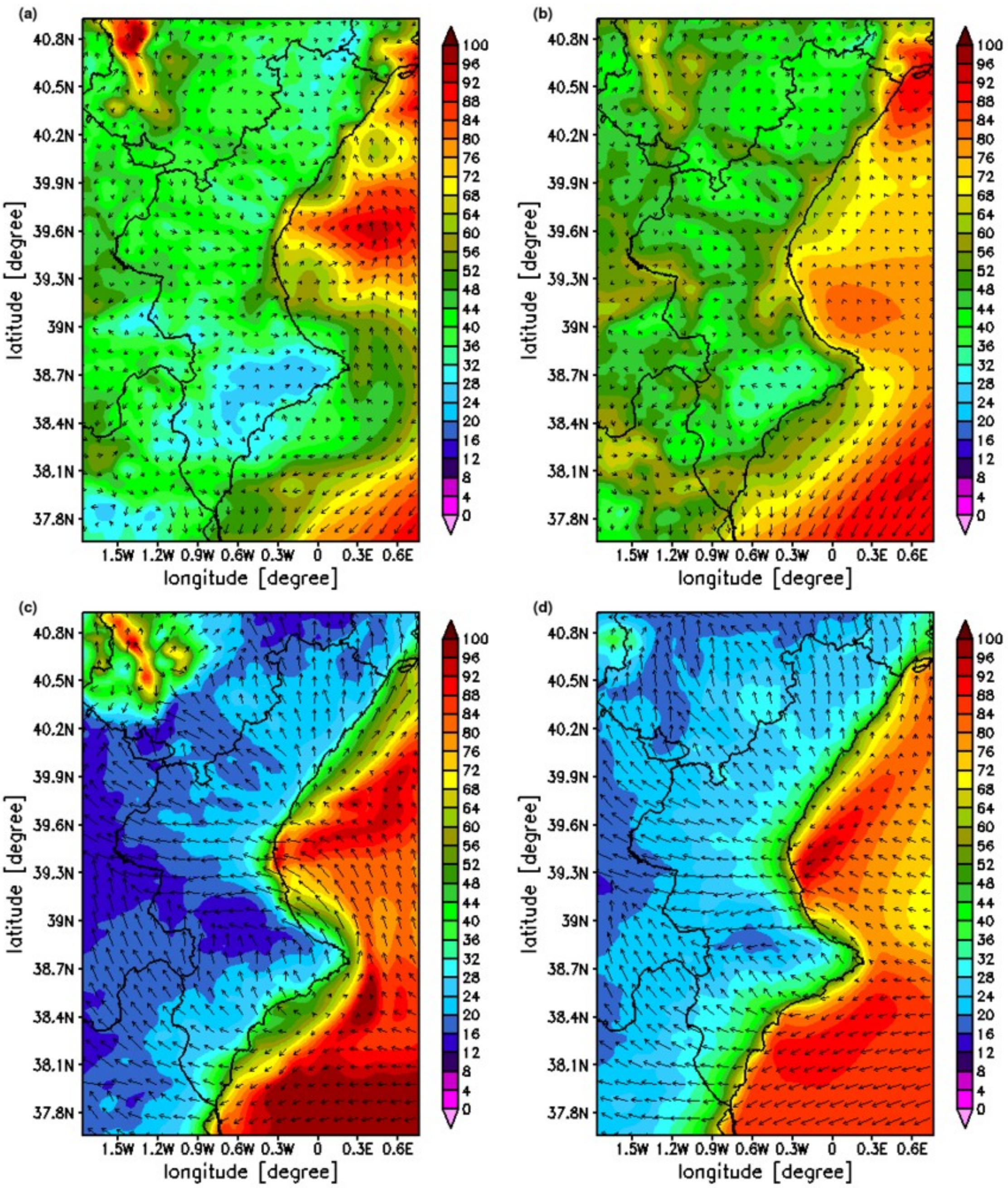
(a)
(b)
(c)
(d)
40.8N
40.5N
40.2N
39.9N
39.6N
39.3N
39N
38.7N
38.4N
38.1N
37.8N
latitude [degree]
1.5W 1.2W 0.9W 0.6W 0.3W 0 0.3E 0.6E
longitude [degree]
100
96
92
88
84
80
76
72
68
64
60
56
52
48
44
40
36
32
28
24
20
16
12
8
4
0

Figure 8

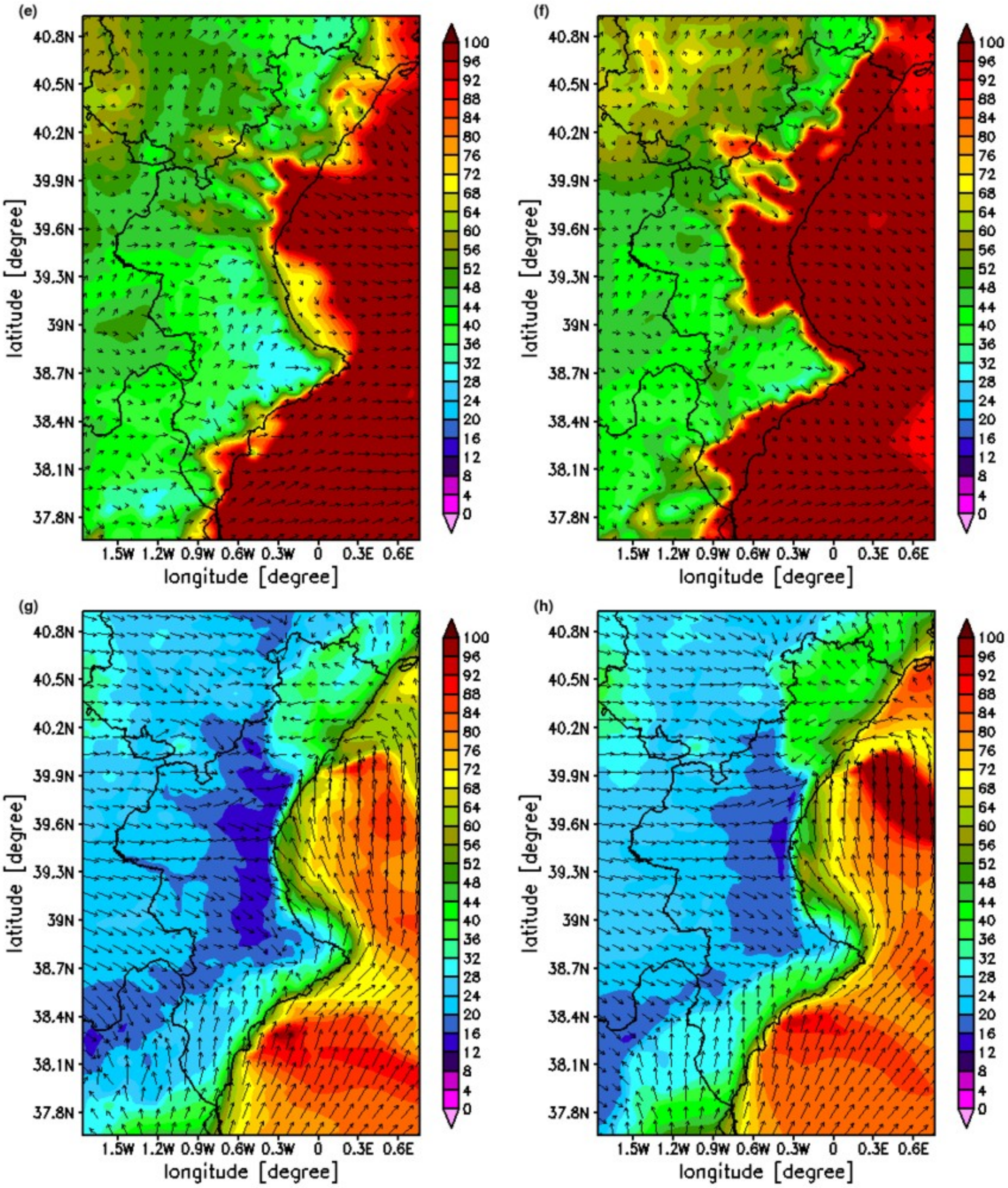

Figure 8 (continued)

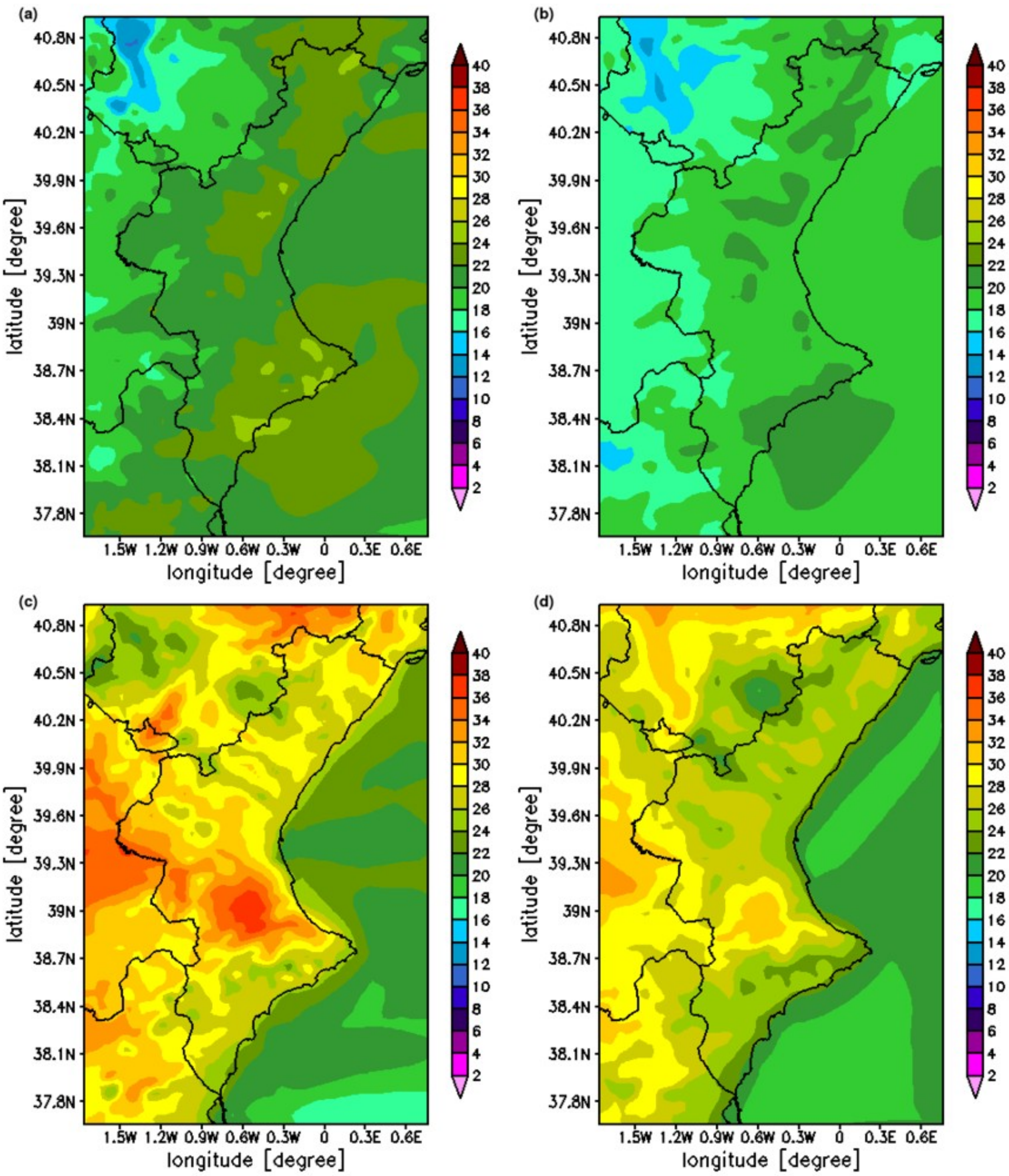
(a)
(b)
(c)
(d)
40.8N
40.5N
40.2N
39.9N
39.6N
39.3N
39N
38.7N
38.4N
38.1N
37.8N
latitude [degree]
1.5W 1.2W 0.9W 0.6W 0.3W 0 0.3E 0.6E
longitude [degree]
40 38 36 34 32 30 28 26 24 22 20 18 16 14 12 10 8 6 4 2

Figure 9

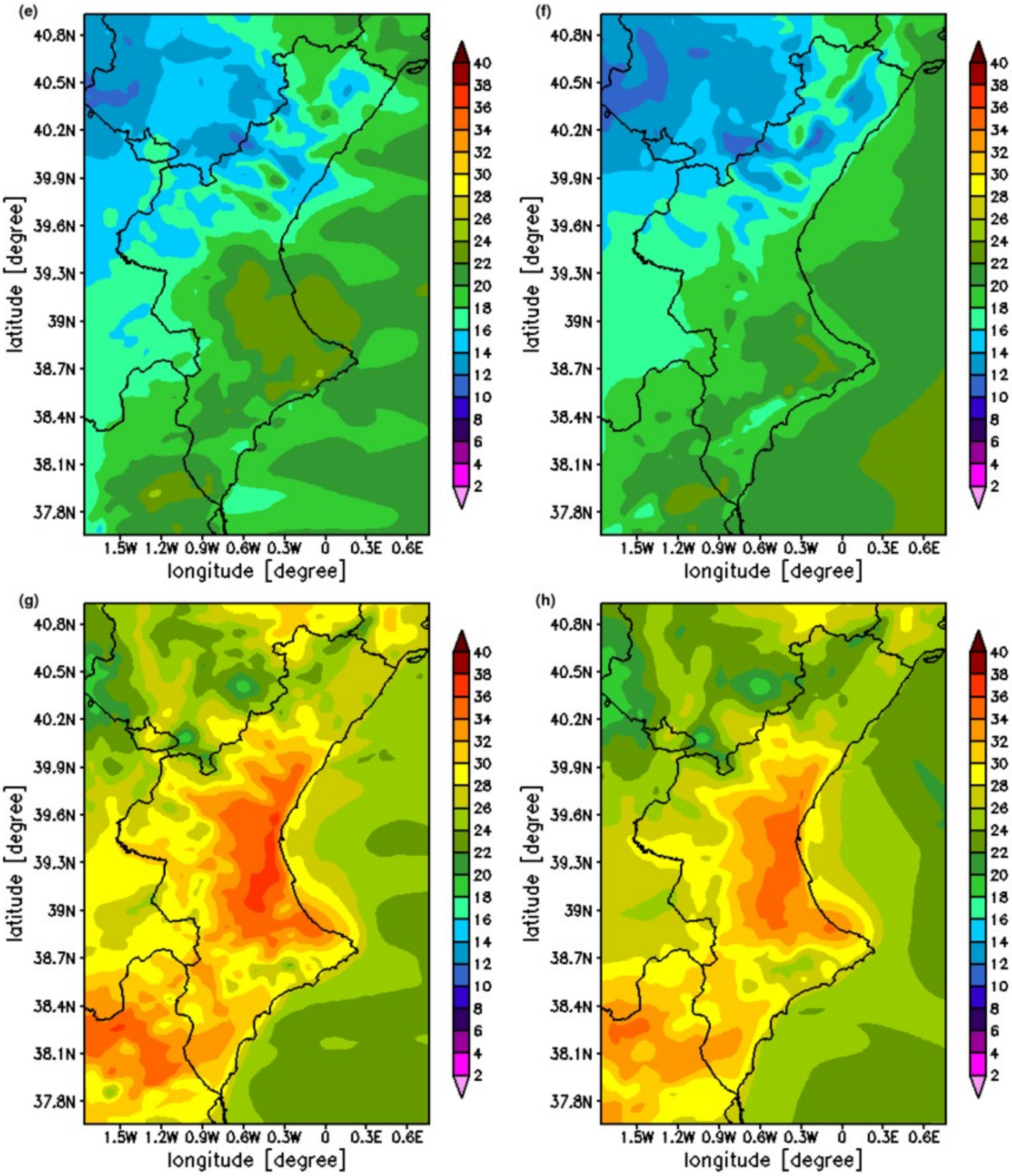

Figure 9 (continued)

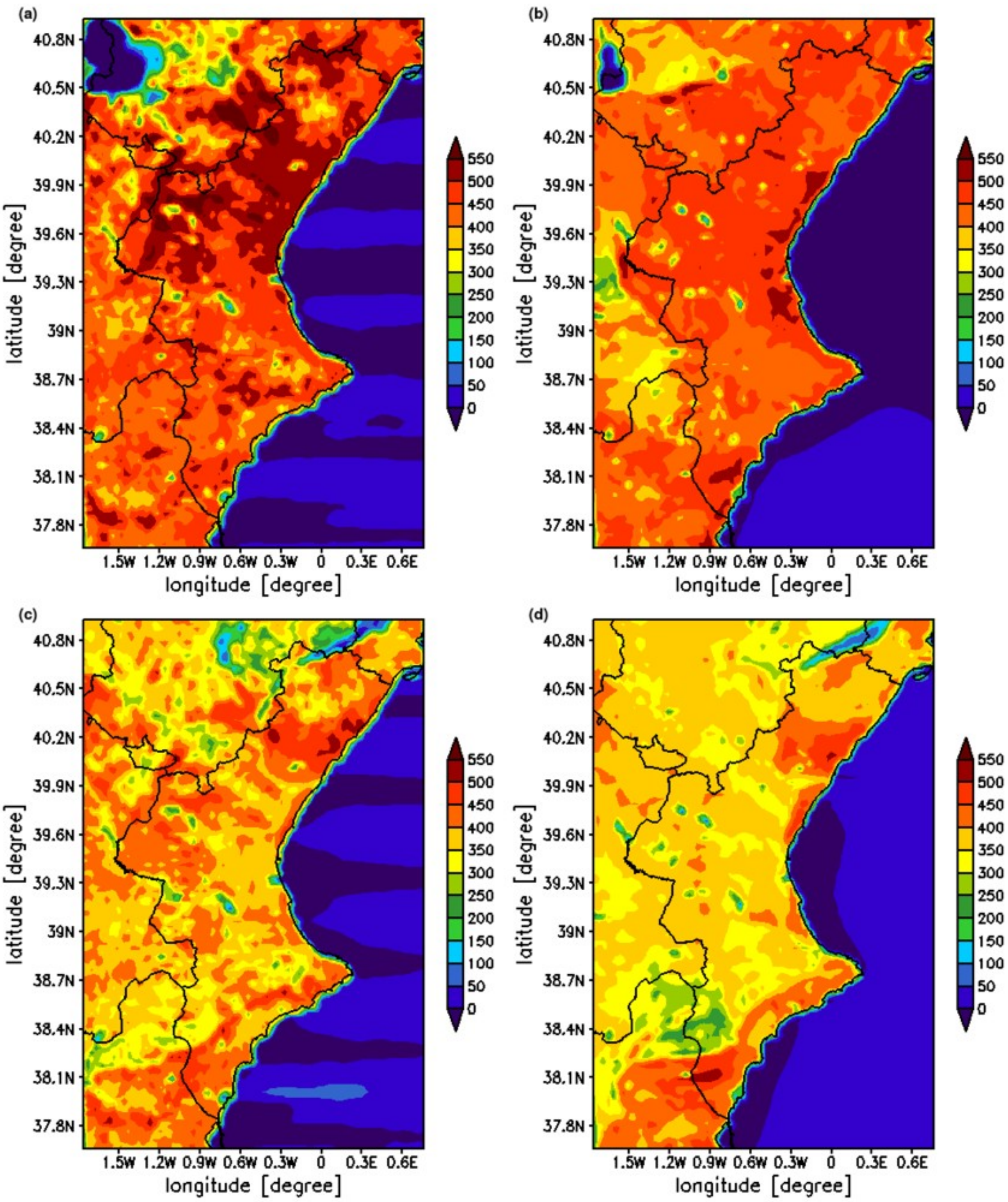
(a)
(b)
(c)
(d)
40.8N
40.5N
40.2N
39.9N
39.6N
39.3N
39N
38.7N
38.4N
38.1N
37.8N
latitude [degree]
1.5W 1.2W 0.9W 0.6W 0.3W 0 0.3E 0.6E
longitude [degree]
550
500
450
400
350
300
250
200
150
100
50
0

Figure 10

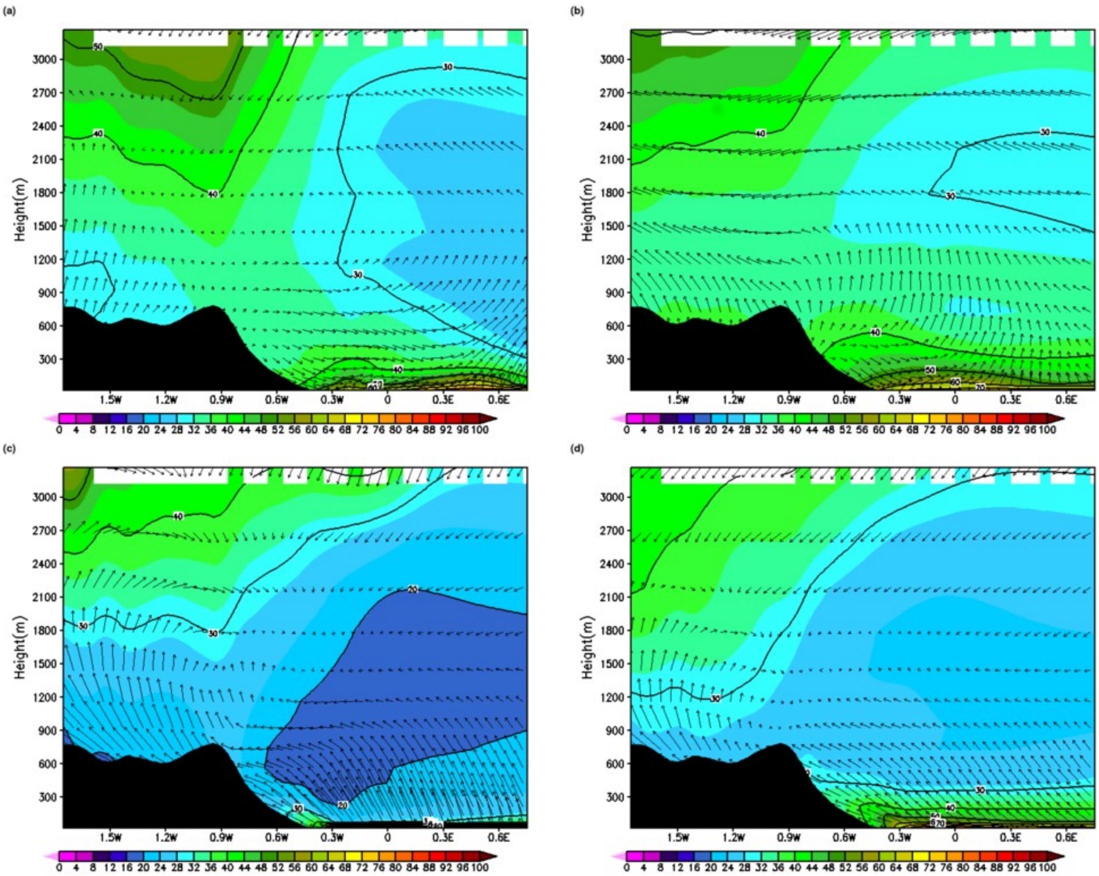
(a)
(b)
(c)
(d)
Height(m)
3000
2700
2400
2100
1800
1500
1200
900
600
300
1.5W
1.2W
0.9W
0.6W
0.3W
0
0.3E
0.6E
0 4 8 12 16 20 24 28 32 36 40 44 48 52 56 60 64 68 72 76 80 84 88 92 96 100

Figure 11

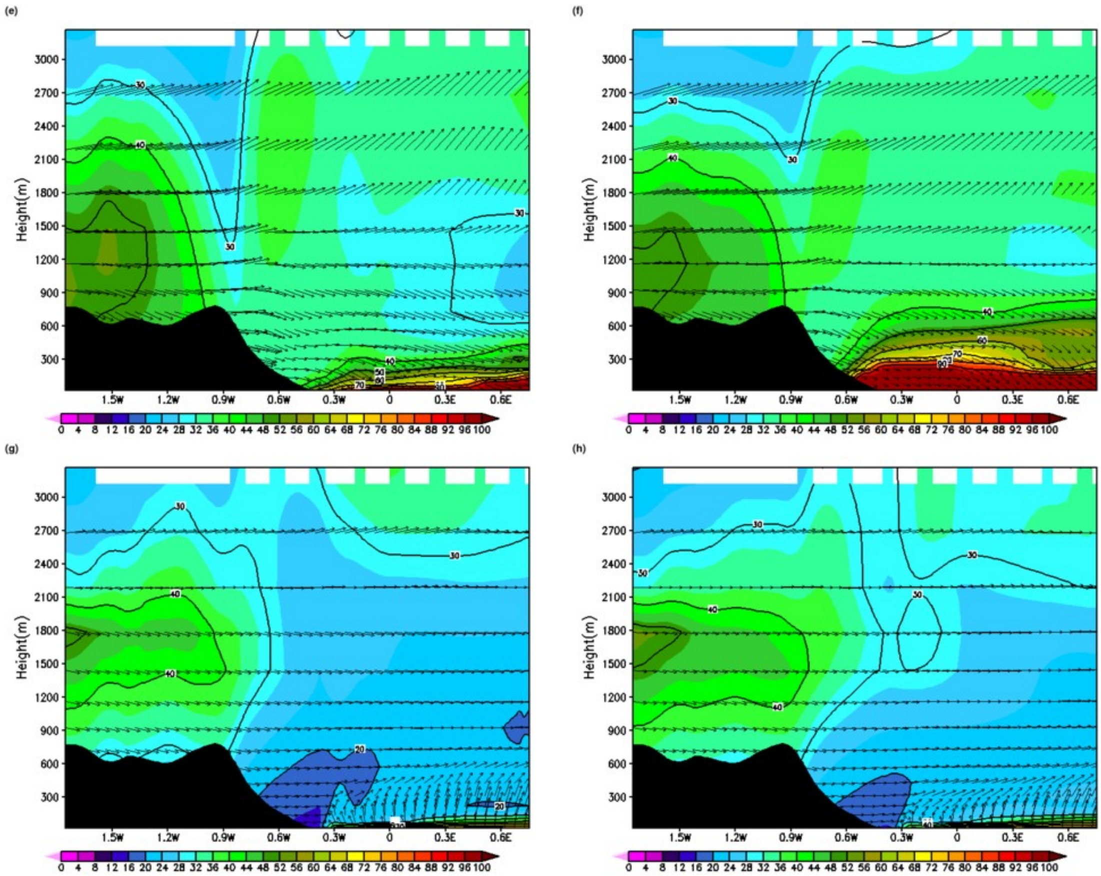

933 Figure 11 (continued)